

Label-free and selective nonlinear fiber-optical biosensing

Johan R. Ott, Mikkel Heuck, Christian Agger, Per D. Rasmussen, and Ole Bang

DTU Fotonik, Department of Photonics Engineering
Technical University of Denmark, 2800 Kongens Lyngby, DK-Denmark
oban@fotonik.dtu.dk

Abstract: We demonstrate that the inherent nonlinearity of a microstructured optical fiber (MOF) may be used to achieve label-free selective biosensing, thereby eliminating the need for post-processing of the fiber. This first nonlinear biosensor utilizes a change in the modulational instability (MI) gain spectrum (a shift of the Stokes- or anti-Stokes wavelength) caused by the selective capture of biomolecules by a sensor layer immobilised on the walls of the holes in the fiber. We find that such changes in the MI gain spectrum can be made detectable, and that engineering of the dispersion is important for optimizing the sensitivity. The nonlinear sensor shows a sensitivity of around 10.4nm/nm, defined as the shift in resonance wavelength per nm biolayer, which is a factor of 7.5 higher than the hitherto only demonstrated label-free MOF biosensor.

© 2008 Optical Society of America

OCIS codes: (190.4380) Nonlinear optics, four-wave mixing; (060.2370) Fiber optics sensors; (060.4005) Microstructured fibers; (280.1415) Biological sensing and sensors

References and links

1. M. E. Bosch, A. J. R. Sanchez, F. S. Rojas, and C. B. Ojeda, "Recent development in optical fiber biosensors," *Sensors* **70**, 797-859 (2007).
2. L. Rindorf, P. E. Hoiby, J. B. Jensen, L. H. Pedersen, O. Bang, and O. Geschke, "Towards biochips using microstructured optical fiber sensors," *Anal. Bioanal. Chem.* **385**, 1370-1375 (2006).
3. X. Fan, I. M. White, S. I. Shopova, H. Zhu, J. D. Suter, and Y. Sun, "Sensitive optical biosensors for unlabeled targets: A review," *Anal. Chimica Acta* **620**, 8-26 (2008).
4. J.-F. Masson, K. Hamersky, S. Beaudoin, and K. S. Booksh, "In vitro biochemical monitoring with fiber optics surface plasmon resonance sensors," *Proc. SPIE* **5261**, 123 (2004).
5. D. A. Markov, K. Swinney, and D. J. Bornhop, "Label-free molecular interaction determinations with nanoscale interferometry," *J. Am. Chem. Soc.* **126**, 16659 (2004).
6. T.-W. Koo, S. Chan, and A. A. Berlin, "Single-molecule detection of biomolecules by surface-enhanced coherent anti-stokes Raman scattering," *Opt. Lett.* **30**, 1024 (2005).
7. Company web site <http://www.resrchintl.com/raptor-detection-system.html>
8. A. Hasegawa and W. F. Brinkman, "Tunable coherent IR and FIR sources utilizing modulational instability," *IEEE J. Quantum. Electron.* **QE-16**, 694-697 (1980).
9. G. P. Agrawal, *Nonlinear Fiber Optics*, 4th edn. (Burlington, MA, USA, 2007).
10. P. M. Moselund, M. Frosz, C. Thomsen, and O. Bang, "Backseeding modulational instability and supercontinuum generation," *Opt. Express* **16**, 11954-11968 (2008).
11. J. E. Sharping, M. Fiorentino, A. Coker, P. Kumar, and R. S. Windeler, "Four-wave mixing in microstructure fiber," *Opt. Lett.* **26**, 1048 (2001).
12. J. E. Sharping, M. Fiorentino, P. Kumar, and R. S. Windeler, "Optical parametric oscillator based four-wave mixing in microstructure fiber," *Opt. Lett.* **27**, 1675-1677 (2002).
13. N. I. Nikolov, T. Sørensen, O. Bang, and A. Bjarklev, "Improving efficiency of supercontinuum generation in photonic crystal fibers by direct degenerate four-wave mixing," *J. Opt. Soc. Am. B* **20**, 2329-2337 (2003).

14. P. St. J Russell, "Photonic crystal fibers," *Science* **299**, 358-362 (2003).
15. R. F. Cregan, B. J. Mangan, J. C. Knight, T. A. Birks, P. St. J. Russell, P. J. Roberts, and D. C. Allan, "Single-mode photonic bandgap guidance of light in air," *Science* **285**, 1537-1539 (1999).
16. J. D. Harvey, R. Leonhardt, S. Coen, G. K. L. Wong, J. C. Knight, W. J. Wadsworth, and P. St. J. Russell, "Scalar modulational instability in the normal dispersion regime by use of a photonic crystal fiber," *Opt. Lett.* **28**, 2225-2227 (2003).
17. T. M. Monro, D. J. Richardson, and P. J. Bennett, "Developing holey fibres for evanescent field devices," *Electron. Lett.* **35**, 1188 (1999).
18. T. M. Monro, W. Belardi, K. Furusawa, J. C. Baggett, N. G. R. Broderick, and D. J. Richardson, "Sensing with microstructured optical fibers," *Meas. Sci. Technol.* **12**, 1854 (2001).
19. J. B. Jensen, L. H. Pedersen, P. E. Hoiby, L. B. Nielsen, T. P. Hansen, J. R. Folkenberg, J. Riishede, D. Noordegraaf, K. Nielsen, A. Carlsen, and A. Bjarklev, "Photonic crystal fiber based evanescent-wave sensor for detection of biomolecules in aqueous solutions," *Opt. Lett.* **29**, 1974-1976 (2004).
20. J. M. Fini, "Microstructure fibres for optical sensing in gases and liquids," *Meas. Sci. Technol.* **15**, 1120-1128 (2004).
21. T. Ritari, J. Tuominen, H. Ludvigsen, J. C. Petersen, H. Sorensen, T. P. Hansen, and H. R. Simonsen, "Gas sensing using air-guiding photonic crystal fibers," *Opt. Express* **17**, 4080-4087 (2004).
22. M. A. van Eijkelenborg, M. C. J. Large, A. Argyros, J. Zagari, S. Manos, N. A. Issa, I. Bassett, S. Fleming, R. C. McPhedran, C. Martijn de Sterke, and N. A. P. Nicorovici, "Microstructured polymer optical fibre," *Opt. Express* **9**, 319-327 (2001).
23. M. C. J. Large, A. Argyros, F. Cox, M. A. van Eijkelenborg, S. Ponrathnam, N. S. Pujari, I. M. Bassett, R. Lwin, and G. W. Barton, "Microstructured polymer optical fibres: New opportunities and challenges," *Mol. Cryst. Liq. Cryst.* **446**, 219-231 (2006).
24. J. B. Jensen, P. E. Hoiby, G. Emiliyanov, O. Bang, L. H. Pedersen, and A. Bjarklev, "Selective detection of antibodies in microstructured polymer optical fibers," *Opt. Express* **13**, 5883-5889 (2005).
25. F. M. Cox, A. Argyros, and M. C. J. Large, "Liquid-filled hollow core microstructured polymer optical fiber," *Opt. Express* **14**, 4135-4140 (2006).
26. G. Emiliyanov, J. B. Jensen, O. Bang, A. Bjarklev, P. E. Hoiby, L. H. Pedersen, E. Kjaer, and L. Lindvold, "Localized biosensing with Topas microstructured polymer optical fiber," *Opt. Lett.* **32**, 460 (2007); erratum *ibid*, 1059 (2007).
27. L. Rindorf and O. Bang, "Sensitivity of photonic crystal fiber grating sensors: biosensing, refractive index, strain, and temperature sensing," *J. Opt. Soc. Am. B* **25**, 310-324 (2008).
28. L. Rindorf, J. B. Jensen, M. Dufva, L. H. Pedersen, P. E. Hoiby, and O. Bang, "Photonic crystal fiber long-period gratings for biochemical sensing," *Opt. Express* **14**, 8224-8231 (2006).
29. F. Kajzar, "Third Harmonic Generation," Chapter 10 in *Characterization Techniques and Tabulations for Organic Nonlinear Optical materials*; M. G. Kuzyk, C. W. Dirk, eds., (Marcel Dekker, Inc., New York 1998).
30. T. M. Monro, Y. D. West, D. W. Hewak, N. G. R. Broderick, and D. J. Richardson, "Chalcogenite holey fibres," *Electron. Lett.* **36**, 1998-2000 (2000).
31. J.-J. Gau, E. H. Lan, B. Dunn, C.-M. Ho, and J. C. S. Woo, "A MEMS based amperometric detector for *E. Coli* bacteria using self-assembled monolayers," *Biosens. Bioelectron.* **16**, 745-755 (2001).
32. L. Rindorf and O. Bang, "Highly sensitive refractometer with a photonic-crystal-fiber long-period grating," *Opt. Lett.* **33**, 563-565 (2008).
33. IAPWS 5C: "Release on refractive index of ordinary substance as a function of wavelength, temperature and pressure" (September 1997) published by International Association of the Properties of Water and Steam (IAPWS). In this work a temperature of $T = 293.15\text{K}$ and a density of water of $\rho = 1000\text{kg}\cdot\text{m}^{-3}$ has been used.
34. Comsol Multiphysics finite element package, <http://www.comsol.com>.
35. M. H. Frosz, T. Sorensen, and O. Bang, "Nano-engineering of a photonic crystal fiber for supercontinuum spectral shaping," *J. Opt. Soc. Am. B* **23**, 1692-1699 (2006).
36. P. D. Rasmussen, J. Laegsgaard, and O. Bang, "Degenerate four wave mixing in solid core photonic bandgap fibers," *Opt. Express* **16**, 4059-4068 (2008).
37. J. M. Dudley, G. Genty, and S. Coen, "Supercontinuum generation in photonic crystal fiber," *Rev. Mod. Phys.* **78**, 1135-1184 (2006).
38. S. Coen, A. H. L. Chau, R. Leonhardt, J. D. Harvey, J. C. Knight, W. J. Wadsworth, and P. St. J. Russell, "Supercontinuum generation by stimulated Raman scattering and parametric four-wave mixing in photonic crystal fibers," *J. Opt. Soc. Am. B* **19**, 753-764 (2002).
39. M. H. Frosz, O. Bang, and A. Bjarklev, "Soliton collision and Raman gain regimes in continuous-wave pumped supercontinuum generation," *Opt. Express* **14**, 9391-9407 (2006).

1. Introduction

Fiber-optical biosensors have a huge potential for providing simple, rapid, and continuous in situ monitoring of biomolecules in the biomedical, pharmaceutical, environmental, defense, bioprocessing, and food technology areas [1]. Low-loss delivery of laser light, long interaction lengths, low fabrication costs, and the ability to both excite target molecules and capture their emitted light, are important advantages of optical fibers in the context of biosensing. Despite their geometry, optical fibers may also be incorporated into disposable lab-on-a-chip biosensors, as the key sensing element [2]. The major goal in the field is to develop fiber-optical biosensors capable of performing rapid and reliable *selective* immunoassays on *unlabeled* samples [3]. Fiber-optical biosensors still have a hard time reaching the levels of sensitivity that are today possible with biosensors based on for example surface plasmons [4], interferometry [5], and surface-enhanced coherent anti-stokes Raman scattering (CARS) [6]. All these methods are label-free and highly sensitive, with CARS even being able to measure single molecules [6]. Nevertheless, the first fiber-optical biosensors are finding their way onto the market, such as the portable multi-analyte RAPTOR [7] with only 10 min. processing time for detection of a bio-agent, thereby underlining the special strengths of the fiber-optical biosensor.

There are an immense number of different configurations and working principles of fiber-optical biosensors (see [1] and [3] for recent reviews). Fluorescence based fiber-optical biosensors may be formally label-free by having the label molecules attached to the probe instead of the sample, such as in the RAPTOR [7]. However, typical fiber-optical label-free biosensors track the change of a resonance (grating, surface plasmon, two-core coupling, Fabry-Perot, etc.) introduced by the presence of a biological agent [3]. Such sensors are truly label-free in that they require no labelled molecules at all, thereby greatly simplifying the biochemistry. Common to them all is that they are linear, in the sense that they use only the linear material properties of the optical fiber. This means that to achieve label-free sensing, postprocessing of the fiber must be performed, such as grating writing, cladding etching to expose the core, layer deposition, femtosecond laser direct writing, etc. Here we present the first *nonlinear* fiber-optical biosensor, which uses the inherent nonlinearity of the fiber material and therefore does not require any postprocessing to achieve truly label-free selective detection of biomolecules.

The working principle of our nonlinear sensor is to track the Stokes and anti-Stokes lines generated by a temporally broad pump laser through the fundamental nonlinear effect of modulational instability, (MI) also known as degenerate four-wave mixing (FWM) [9, 8]. As such our sensor is also tracking a resonance, since MI is a nonlinear resonant effect, requiring phase-matching between two pump photons and the Stokes and anti-Stokes photons. Through the resonant phase-matching condition the Stokes and anti-Stokes wavelengths depend strongly on the fiber dispersion. We use this and determine the sensor configuration that optimizes the influence of a captured layer of biomolecules on the geometrical part of the fiber dispersion. Immediate design considerations are: The fiber should be short to minimize sample volume, which means that the MI gain must be strong. The MI process can be artificially seeded through, e.g., coupling back part of the output [10]. However, to keep the sensor simple, we here consider only unseeded MI. Effective unseeded MI requires that the fiber has zero dispersion close to the pump [11, 12, 13] and that the effective nonlinearity γP_0 is strong. Here P_0 is the pump peak power and γ is the nonlinearity coefficient, which is proportional to the material nonlinearity and inverse proportional to the effective area of the fiber [9].

The fiber we use is a microstructured optical fiber (MOF), which has a pattern of air holes running along the entire length of the fiber [14]. The optical properties of the fiber are primarily determined by the position, size, and shape of the air holes and MOFs exhibit a number of unique properties compared to conventional step-index fibers. The MOF can be designed to guide in air through the photonic bandgap effect [15]. However, here we want to use the fiber

nonlinearity, and thus bandgap MOFs are not directly applicable. We use the solid-core index-guiding MOF, because it has a number of advantageous properties for our nonlinear biosensor: First of all the holey cladding allows us to perform bio-chemical reactions and define sensor layers inside the air holes in close proximity to the fiber core. Biological samples may hence be probed by the optical field without removing the fiber coating and cladding, thus maintaining the robustness of the fiber. The holes in the cladding are small and thus only minute sample volumes are required (nanoliter regime). The solid-core index-guiding MOF is also ideal for MI [11, 12, 16], because the zero-dispersion wavelength (ZDW) is widely tunable and because the fiber core may be made extremely small, thereby increasing the effective nonlinearity.

Evanescent wave sensing with silica MOFs was first proposed by Monro *et al.* [17, 18] and it was later demonstrated that DNA in aqueous solution could be detected using fluorescence [19]. Filling bandgap MOFs with sample liquids the optical field can be guided in the core, and thus directly in the sample, significantly increasing the overlap between the optical field and the sample, with obvious advantages for sensing [20, 21]. Polymer MOFs (or mPOFs) are now routinely fabricated with a wealth of different hole-structures [22, 23], primarily in polymethylmethacrylate (PMMA). PMMA is much easier to functionalize than silica and thus PMMA mPOFs are very appropriate for biosensing [24, 25]. Recently Topas mPOFs have been drawn and demonstrated to have advantageous properties for fiber drawing and biosensing [26]. Because of the nature of the evanescent wave being strongest at the hole surface and decaying rapidly inside the holes, it is possible to sense biomolecular layers attaching to the hole surface, rather than sensing the average index of the material in the holes [27]. Although many MOF sensors have been demonstrated experimentally, it has not been in the context of label-free biosensing. The only demonstration of label-free biosensing was using a silica MOF with a long-period grating (LPG) to measure the thickness of double-stranded DNA [28]. Note that this experiment did not show *selective* biosensing, but label-free measurements of the thickness of biomolecules. A shift of 1.4nm in the LPG resonance wavelength per nm of double-stranded DNA layer was demonstrated, henceforth defined as a sensitivity of 1.4nm/nm. Here we show, using the same material, that our label-free and selective nonlinear biosensor can have a sensitivity more than 7 times higher.

The choice of fiber material is important and primarily determined by the operating wavelength and the required strength of the nonlinearity. Silica MOFs have low loss out to about $2\mu\text{m}$ and the zero-dispersion wavelength can be tuned from below 550nm to above 1550nm. However, the nonlinearity is low. The nonlinearity of standard PMMA mPOFs is $n_2 = 1.5 \times 10^{-19} \text{m}^2/\text{W}$ [29], which is a factor of 6 stronger than that of silica, and the dispersion is comparable to silica. Thus mPOFs could be relevant for our nonlinear biosensor. However, polymer is not good at handling high power and one needs to take into account the huge and strongly wavelength dependent loss typical for mPOFs above 700nm. Another potentially suitable fiber material is the highly nonlinear soft glasses, with nonlinearity a factor of 100-1000 times that of silica. Soft glass MOFs are now routinely fabricated [30] and they guide very well at longer wavelengths. However, these fibers are quite lossy at visible wavelengths and difficult to fabricate with zero dispersion below 1300nm.

In this first proof-of-principle we have chosen silica as the fiber material. This is the most mature technology and the same material as the MOF used in the so far only experimentally demonstrated label-free MOF biosensor [28]. Thus we can make a fair comparison with the 1.4nm/nm sensitivity obtained in [28]. Furthermore, we want to use a 1064nm picosecond (ps) pump laser, because it is readily available to us in an all fiber configuration with average output powers up to tens of Watts. This means that we want low loss and ZDW at 1064nm, which is now standard with silica MOFs. However, we also want ZDW at 1064nm with water in the holes, as we always consider the sensor operating in both an air-configuration, in which air

is blown through the holes after sampling, leaving the holes filled with air, and in a water-configuration, in which water is flushed through after sampling, leaving the holes filled with water. We initially study in detail the application of a commercial MOF with a triangular hole structure (henceforth denoted triangular MOF) and then go on to optimize the triangular hole structure for this particular sensor purpose, before checking the predicted optimum sensor operation with full numerical modelling.

2. Sensor configuration and sample specifications

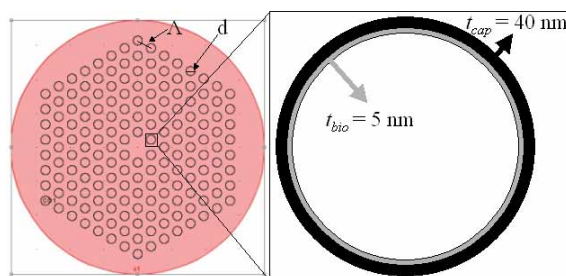


Fig. 1. Left: Triangular MOF with pitch, Λ , and hole diameter, d . Right: Hole with sensor layer of thickness t_{cap} having captured a layer of biomolecules of thickness t_{bio} . In this work $t_{cap} = 40\text{nm}$ and $t_{bio} = 5\text{nm}$. Both layers are assumed to have a refractive index of $n = 1.45$ and no material dispersion.

In this work we use as the sensing element a standard index guiding triangular silica MOF with pitch, Λ , and hole diameter, d , as illustrated in Fig. 1. We assume that inside the holes a sensor layer of thickness t_{cap} has been immobilized onto the walls. This sensor layer can capture a layer of biomolecules of thickness t_{bio} through a selective biochemical process. In this proof-of-principle we want to consider nice big molecules to be able to have a detectable effect. We therefore design our sensor for detection of antibodies, such as α -streptavidin, through the well-known and highly selective antigen-antibody binding process [24, 26]. The α -streptavidin antibody has a typical size of $10 \times 10 \times 10 \text{ nm}$, whereas the streptavidin antigen has a typical size of $5.5 \times 4.5 \times 4.5 \text{ nm}$ [31]. Streptavidin does not bind directly to silica and thus additional layers are necessary for defining the sensor layer [28]. We therefore fix the thickness of the combined sensor layer (streptavidin plus activating intermediate layers) to be $t_{cap} = 40 \text{ nm}$ and choose a worst case scenario for the thickness of the captured biolayer with $t_{bio} = 5 \text{ nm}$. The refractive index and material dispersion of the biolayers will depend on how the biomolecules are oriented. Here we neglect the dispersion of the biolayers and assume that they have the same refractive index of 1.45, close to that of silica. Our argument for this assumption is that experiments with PCF biosensors have showed that assuming a refractive index of about 1.45 of molecules, such as double-stranded DNA and poly-L-lysine, could reproduce known measurements of the size of these molecules [28]. Naturally, when our proposed biosensor is demonstrated experimentally, this assumption should be tested.

Note that as such the sensor we propose may equally well be applied to refractive index sensing, just as for example MOF sensors based on Bragg or long-period grating [27], where very sensitive refractometers may be obtained [32].

The introduction of samples in aqueous solution into the sensor might leave remnants of water, which is difficult to remove. For a given fiber we therefore always consider two sensor configurations: The air-configuration, in which air is blown through the holes after sampling,

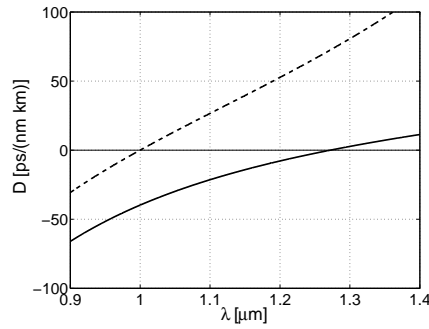


Fig. 2. Material dispersion of silica with ZDW at 1272.7nm (solid) and water with ZDW at 1000.2nm (dashed). The dispersion at 1064nm is -27.4ps/(nm·km) for silica and 17.2ps/(nm·km) for water.

leaving the holes filled with air. The water-configuration, in which water is flushed through after sampling, leaving the holes filled with water. For the refractive index of water the wavelength dependence has been included [33], while that of air is neglected. The material dispersion of silica and water is shown in Fig. 2.

We first consider a specific sensor using a commercially available triangular MOF from Crystal Fibre A/S, which has a pitch of $\Lambda = 3.45\mu\text{m}$ and a hole diameter of $d = 1.7\mu\text{m}$. In the following this fiber is referred to as the Highly NonLinear (HNL) fiber. The HNL fiber is chosen because it has a reasonable high nonlinearity and because it is specified to have ZDW around 1060nm, where we would like to pump. The dispersion profiles of the clean HNL fiber, the sensor, and the activated sensor have been calculated using COMSOL [34]. By activated sensor we here and in the following mean a sensor (MOF with sensor layer of thickness $t_{\text{cap}} = 40\text{nm}$), which has captured a layer of antibodies of thickness $t_{\text{bio}} = 5\text{nm}$. The results are shown in Fig. 3 for both the air- and water-configurations.

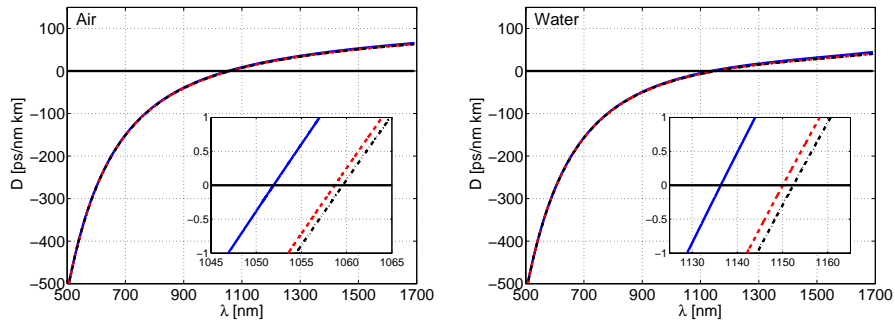


Fig. 3. Dispersion of the HNL fiber with pitch $\Lambda = 3.45\mu\text{m}$ and hole size $d = 1.7\mu\text{m}$ (blue solid), the HNL fiber with a 40nm sensor layer (red dashed), and the HNL fiber with a 40nm sensor and a 5nm antibody layer (black dash-dotted). Left: Dispersion with air in the holes. Right: Dispersion with water in the holes.

Our numerical results confirm a ZDW of around 1060nm for the HNL fiber with air in the holes. The introduction of water in the fiber increases the effective refractive index of the guided mode and pushes the ZDW to around 1140nm, which means that the pump at 1064nm is suddenly in the normal dispersion regime. This has severe implications for a sensor using the HNL

fiber and pumping at 1064nm, as we will show in the following. The addition of the 5nm antibody layer does not seem to change the dispersion significantly. However, even small changes in the dispersion can lead to strong changes in the MI gain spectrum [13, 35] as we will see in the following, where we introduce MI as the sensing mechanism and detail the sensor operation.

3. Sensing mechanism - modulational instability

The detection mechanism of our biosensor is based on MI, also known as degenerate FWM, where two pump photons of frequency ω generates a Stokes photon with frequency ω_S and an anti-Stokes photon with frequency ω_{aS} . Due to energy conservation the two new photons are generated symmetrically around the pump, with the Stokes photon being down-shifted, $\omega_S = \omega - \Omega$, and the anti-Stokes photon being up-shifted, $\omega_{aS} = \omega + \Omega$. MI thus generates side bands around the pump, centered at the Stokes and anti-Stokes frequencies. The idea is that if a given sample contains our target biomolecules, then the sensor layer will capture a layer of thickness t_{bio} of these biomolecules, which will change the cladding structure, e.g., by reducing the hole diameter. This will influence the dispersion and the effective area, A_{eff} , which in turn will move the Stokes and anti-Stokes lines, leading to a detection by tracking this change.

The MI gain is given by [9]

$$g(\Omega) = \sqrt{(\gamma P_0)^2 - (\kappa/2)^2}, \quad \kappa = 2\gamma P_0 + \Delta\beta \quad (1)$$

where $\gamma = n_2\omega_0/(cA_{eff})$ is the nonlinear parameter, c is the speed of light in vacuum, ω_0 is the pump frequency, $n_2 = 2.6 \times 10^{-20} \text{m}^2/\text{W}$ is the nonlinear refractive index of Silica, P_0 is the peak power of the pump, and A_{eff} is the effective area of the guided mode, here assumed not to vary with wavelength. The maximum MI gain, $g_{max} = \gamma P_0$, is independent of the dispersion and occurs at phase-matching, $\kappa = 0$, which corresponds to the linear phase-mismatch $\Delta\beta = \beta(\omega_S) + \beta(\omega_{aS}) - 2\beta(\omega) = -2\gamma P_0$, where $\beta(\omega)$ is the linear propagation constant at the frequency ω . Using a Taylor expansion of $\beta(\omega)$ the linear phase-mismatch is given by [9]

$$\Delta\beta = \sum_{m=1}^{\infty} \frac{\beta_{2m}}{(2m)!} \Omega^{2m}, \quad \beta_m \equiv \left. \frac{\partial^m \beta}{\partial \omega^m} \right|_{\omega=\omega_0}, \quad (2)$$

from which we see that only even order dispersion coefficients, β_{2m} , influence the MI gain.

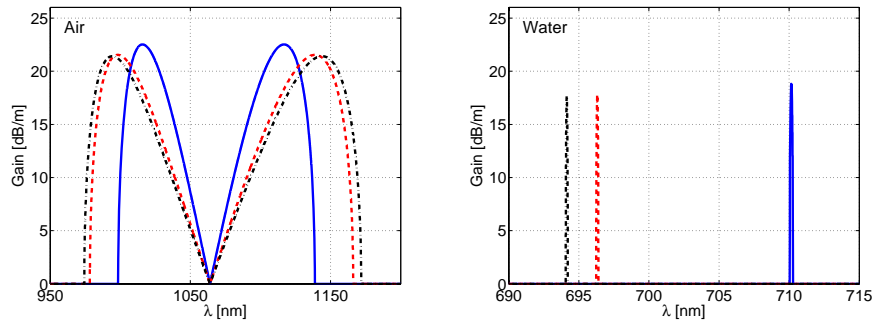


Fig. 4. Gain spectra of the HNL fiber with pitch $\Lambda = 3.45\mu\text{m}$ and hole size $d = 1.7\mu\text{m}$, pumped at $\lambda = 1064\text{nm}$ with peak power $P_0 = 500\text{W}$. Clean HNL fiber (blue solid), HNL fiber with a 40nm sensor layer (red dashed), and HNL fiber with a 40nm sensor and a 5nm antibody layer (black dash-dotted). Left: gain spectrum with air in the holes. Right: gain spectrum with water in the holes and only the anti-Stokes band shown.

With only 2nd order dispersion, β_2 , MI requires anomalous dispersion, $\beta_2 < 0$, and only one set of gain bands exist close to the pump [8, 11, 12]. However, in MOFs, with significant higher order dispersion, MI can also occur when pumping in the normal dispersion regime, in which case the gain bands are narrow and further from the pump [16]. In bandgap fibers the strong higher-order dispersion can even lead to the generation of Stokes and anti-Stokes waves across bandgaps [36]. In index-guiding PCFs the gain bands appearing in the anomalous and normal dispersion regimes are actually representative for the MI gain bands of our HNL sensor in the air and water configurations, respectively, when pumped at 1064nm, as can be seen in Fig. 4. The narrow gain bands of the water configuration will be extremely difficult to detect and might even disappear completely in a real fiber, due to small fluctuations in the fiber parameters along the fiber [13]. Thus, even before considering the wavelength shifts, the water configuration with the HNL fiber pumped at 1064nm can be discarded. In the following we detail the sensor operation in terms of the MI gain and the shifts in the Stokes and anti-Stokes wavelengths that occur when the sensor captures a 5nm layer of biomolecules.

4. Sensor operation with commercial HNL fiber

Using the commercially available finite element tool COMSOL [34] MOFs with a triangular hole structure have been implemented so that the pitch, Λ , and hole diameter, d , were adjustable. The propagation constant, β , was calculated for 150 different pump wavelengths in the range 500-1700nm. A fit to a polynomial of degree 15 was used to derive the ω -dependence of β , from which we found the coefficients, β_m . These coefficients were then used to calculate the dispersion and gain spectra of the specific fibers, such as those shown in Figs. 3 and 4. In this section we use as sensor fiber the commercial HNL fiber.

Let us first consider the air-configuration, pumped at 1064nm with peak power 500W. From Fig. 3 we see that the ZDW for the clean HNL fiber is 1051.9nm. Adding the 40nm sensor layer shifts the ZDW by 6.8nm and capturing the 5nm layer of target biomolecule shifts the ZDW by an additional 0.9nm to 1059.6nm. From Fig. 4 we see that because the pump is close to the ZDW in all three cases, the Stokes and anti-Stokes gain bands are wide and close to the pump. From Fig. 4 we see that capturing the target molecules results in a shift of the Stokes (anti-Stokes) wavelength by 5.1nm (3.9nm). This gives a sensitivity of 1.0nm/nm, which is a little less than the benchmark of 1.4nm/nm obtained with a long-period grating in [28].

In the corresponding water configuration we see from Fig. 3 that the ZDW of the clean HNL fiber is now 1136.3nm and shifts by 13.8nm and 2.3nm when the sensor layer and the biolayer are added, respectively. The pump is now in the normal regime far from the ZDW and correspondingly we see in Fig. 4 that the gain bands are extremely narrow and far from the pump. Only the anti-Stokes lines around 700nm are shown, whereas the Stokes lines around $2.2\mu\text{m}$ are not shown. The anti-Stokes shift obtained when capturing the biolayer is only 2.2nm.

The HNL fiber in the water configuration is clearly not suitable for sensing, at least when pumping at 1064nm. The gain bands are too narrow and will most probably be averaged out in a real fiber due to fluctuations. In addition the Stokes line is out at $2.2\mu\text{m}$ where conventional detectors are not available and where the material loss of Silica is starting to be significant. The air-configuration could be suitable, but further optimization would be needed.

Given the HNL fiber as the sensing element, we can still tune both the pump power and to some degree the pump wavelength in order to optimize the sensitivity. In Fig. 5 we show how the Stokes (blue) and anti-Stokes (red) wavelengths depend on the pump wavelength. The ZDW of the sensor, λ_{cap} , and the activated sensor, λ_{bio} , are shown as vertical solid lines. The MI based sensor is clearly highly tunable in the sense that with only slight changes in the pump wavelength one can significantly tune the sensing wavelength, i.e., the Stokes and anti-Stokes wavelengths. This is an inherent property of MI when pumping close to the ZDW. The Stokes

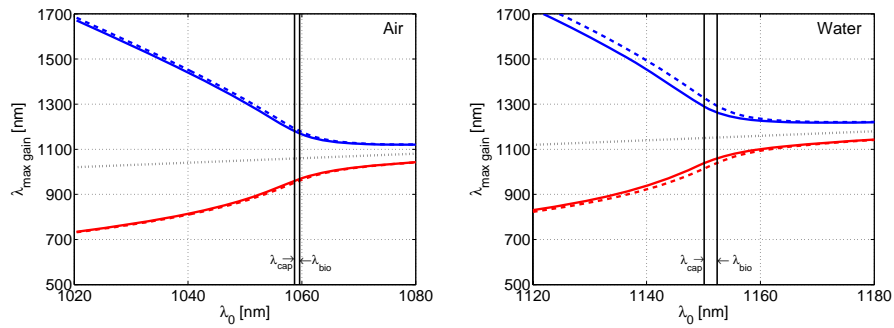


Fig. 5. Stokes and anti-Stokes wavelengths vs. pump wavelength for the HNL fiber with peak power $P_0 = 500\text{W}$. Vertical lines mark the ZDW of the sensor, λ_{cap} , and the activated sensor, λ_{bio} . Solid (dashed) lines show the Stokes and anti-Stokes wavelengths of the sensor (activated sensor). The black dotted line indicates the pump wavelength. Blue (red) color indicates the Stokes (anti-Stokes) peak. Left: Air in the holes. Right: Water in the holes.

wavelength is seen to rapidly move away from the pump wavelength as the pump is moved further into the normal dispersion region. Thus, when pumping at 1064nm, the sensor configuration with water in the holes cannot use the Stokes band for detection, as already discussed. However, pumping around 1150nm, the water-configuration could be applicable.

The actual shift, and thus the sensitivity, is not visible in Fig. 5. We therefore show this separately in Fig. 6, where the ZDW of the clean HNL fiber, λ_z , is also included for reference, along with those of the sensor and the activated sensor. The largest shift due to the capture of the biolayer is seen to occur when pumping just inside the normal dispersion region of the sensor and it always occurs for the Stokes line. Thus a maximum shift of 13nm can be obtained for the Stokes line in the air-configuration (pumping at optimum 1054nm), whereas a huge 43nm shift can be obtained for the Stokes line in the water-configuration (pumping at optimum 1146nm). The much larger shift with water in the holes is explained by the smaller slope of the dispersion curve (see Fig. 3) giving a steeper slope of the Stokes and anti-Stokes wavelengths as function of pump wavelength (see Fig. 5). A shift of 43nm would give a sensitivity of 8.6nm/nm, which is more than a factor of 6 higher than in [28].

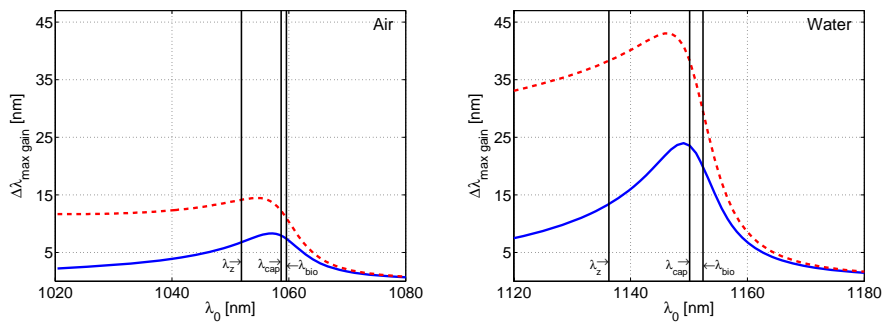


Fig. 6. Wavelength shift vs. pump wavelength for the HNL fiber with peak power $P_0 = 500\text{W}$. The red dashed (blue solid) line shows the shift of the Stokes (anti-Stokes) peak. Vertical lines mark the ZDW of clean fiber, λ_z , the sensor, λ_{cap} , and the activated sensor, λ_{bio} . Left: Air in the holes. Right: Water in the holes.

Before getting all excited we need to consider the gain in the MI process, since our sensor fiber cannot be too long in order to limit the sample volume. The maximum gain of the activated sensor, when pumping at 1064nm with 500W, is seen to be 22.0dB/m for the air-configuration and 17.5dB/m for the water configuration. The difference in gain is because the different structures have different effective areas, A_{eff} . If we want a maximum fiber length of say 50cm, then about 20dB/m might not be enough to obtain a detectable signal. From Eq. (1) we know that the maximum gain $g_{\text{max}} = \gamma P_0$ is proportional to the pump peak power. However, the phase-mismatch, κ , and thus the Stokes and anti-Stokes wavelengths, also depend on the power. In Fig. 7 we therefore detail the dependence of the sensor on the pump power. We choose the air-configuration and pump at $\lambda_0 = 1054\text{nm}$, at which the peak sensitivity of 13nm is obtained. The dependence for the water configuration with maximum sensitivity is qualitatively the same and therefore not shown.

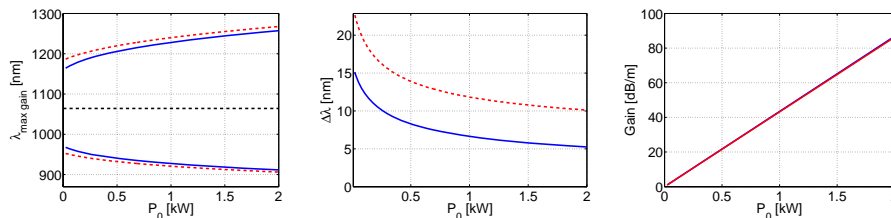


Fig. 7. Influence of peak pump power P_0 for the HNL fiber with air in the holes and pumping at $\lambda_0 = 1054\text{nm}$. Left: Stokes and anti-Stokes wavelengths of sensor (solid blue) and activated sensor (dashed red). Middle: shift of Stokes (dashed red) and anti-Stokes (solid blue) wavelengths. Right: maximum gain of sensor (solid blue) and activated sensor (dashed red).

In Fig. 7 the linear dependence of the maximum gain on the pump peak power is clearly seen. We also see that as the power is increased the Stokes and anti-Stokes wavelengths move away from the pump and the shift decreases. However, the decrease in the shift saturates and thus it is advantageous to increase P_0 as much as possible, of course without initiating supercontinuum generation and without burning the fiber and destroying the biomolecules.

The initial investigation of the commercial HNL fiber has thus revealed a couple of interesting points. In the air-configuration and pumping around 1054nm with 500W peak power, a shift of about 13nm can be obtained, which is twice the sensitivity obtained in [28]. More importantly, a sensitivity of 43nm could potentially be obtained in the water-configuration, if one could pump at 1146nm. In the following section we optimize the sensor for operation at 1064nm by changing the airhole structure of the MOF. The important point will be whether the huge 43nm shift in the water configuration can be maintained when changing the structure to have ZDW around 1064nm.

5. Optimization of sensitivity for pumping at 1064nm

We now want to optimize the triangular hole pattern of the MOF so as to achieve a maximum shift when pumping at 1064nm. From the study of the HNL fiber we know that the maximum shift occurs when pumping somewhere in between the ZDW of the clean fiber and the ZDW of the sensor. Unfortunately the optical properties and the exact thickness of the biolayers, are not well-defined and depend, e.g., on the orientation of the molecules relative to the hole surface. However, the ZDW of the clean fiber is a well-defined quantity, which is close to the optimum and can be calculated for a given hole structure.

We therefore map out the values of the pitch and hole diameter, for which the MOF has ZDW at 1064nm. To be able to perform biochemical reactions inside the holes and have reasonable

filling times, the hole diameter cannot be too small. From earlier work with filling MOFs with liquid crystals we have found that a minimum hole diameter of $1\mu\text{m}$ is appropriate. For a given value of the hole diameter between $d = 1\mu\text{m}$ and $d = 4\mu\text{m}$ we have calculated the optimum value of the pitch, as the one for which ZDW is 1064nm . The optimum values of the fiber parameters are shown in Fig. 8. Importantly we have found that for hole sizes below $d = 1.75\mu\text{m}$ one cannot achieve ZDW at 1064nm with water in the holes. This is why the curve for water starts at $d = 1.75\mu\text{m}$.

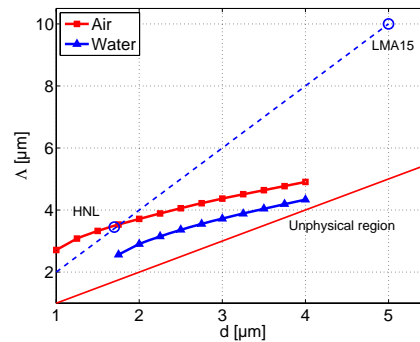


Fig. 8. Hole diameter, d , and pitch, Λ , for which a triangular silica MOF has ZDW at $\lambda_0 = 1064\text{nm}$. The solid red (blue) curve indicates the parameters with air (water) in the holes. Fibers with parameters above (below) this curve have ZDW above (below) $\lambda_0 = 1064\text{nm}$. The solid straight line indicates the boundary $d = \Lambda$, below which the parameters are not physical. The dashed straight going through the HNL parameters indicates a scaling down of the commercial LMA-15 fiber (both indicated with a circle).

Let us first consider the air-configuration: For the set of optimal parameters we plot in Fig. 9 how the effective area, the maximum gain, the Stokes and anti-Stokes wavelengths, and the shift, depend on the hole size of the MOF. As expected we see that the effective area decreases down to about $13\mu\text{m}^2$ as the hole size decreases. This means that the nonlinearity parameter γ increases and thus that the MI gain increases up to a value of about 24dB/m . The obtainable shift increases with a decreasing hole size, which is to be anticipated, because the relative change in the hole size by capturing a 5nm biolayer increases when the hole becomes smaller. The maximum shift of 60nm , obtained for $d = 1\mu\text{m}$, comes with the added benefit of having the largest gain. This is a significant shift, but unfortunately the gain is only 24dB/m .

Let us now consider the water-configuration, for which Fig. 10 shows the optimum sensor parameters as Fig. 9 did for the air-configuration. The trends are here completely the same as with air, with both the gain and the shift increasing as the hole size is decreased. However, already at a hole size of $d = 1.75\mu\text{m}$ the gain is more than 40dB/m and the Stokes shift is 52.2nm , where the corresponding values for air was about 20.6dB/m and 10nm , respectively. Unfortunately, as already discussed, $d = 1.75\mu\text{m}$ is the smallest hole diameter for the water configuration, for which a ZDW of 1064nm can be reached.

The optimization has thus revealed that the largest gain is about 40dB/m , which is obtained in the water configuration. In contrast the largest shift of 60nm in the Stokes wavelength was obtained in the air configuration. However, this large shift was for a small hole size of only $1\mu\text{m}$, for which doing rapid bio-chemical reactions inside the holes could prove problematic. We therefore consider the MOF with $d = 1.75\mu\text{m}$ and $\Lambda = 2.56\mu\text{m}$ in the water configuration as the optimum sensor, for which we predict a gain of 40dB/m and a shift of 52.2nm , corresponding to a sensitivity of 10.4nm/nm , a factor 7.5 better than the hitherto best sensitivity [28]. In the

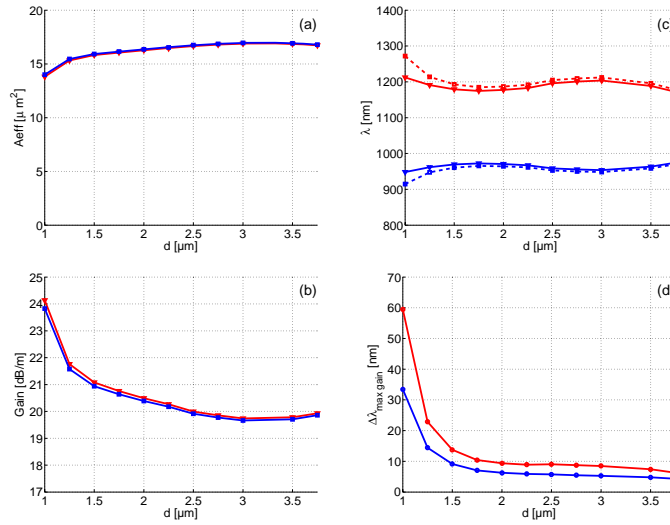


Fig. 9. Sensor parameters vs. hole diameter d for optimized air-configuration when pumping at 1064nm with power $P_0 = 500\text{W}$. (a) Effective area of the sensor (b) Maximum gain of the sensor; (c) anti-Stokes (blue) and Stokes (red) wavelengths for sensor (solid) and activated sensor (dashed); (d) Shift of the anti-Stokes (blue) and Stokes (red) wavelengths.

next section we perform direct numerical modelling to verify the functionality of the sensor.

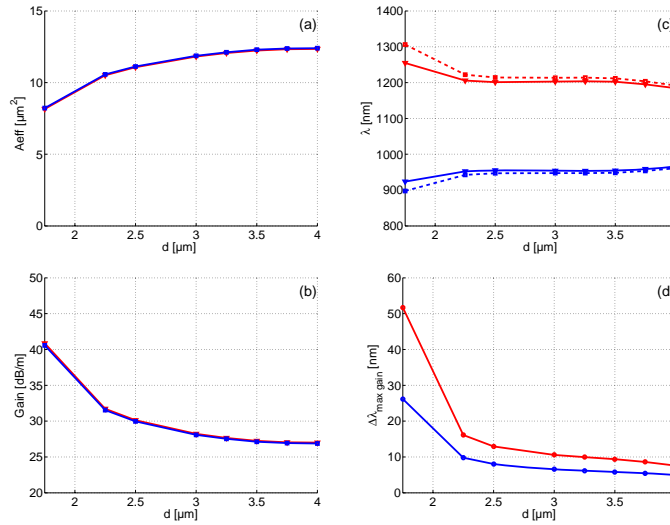


Fig. 10. Sensor parameters vs. hole diameter d for optimized air-configuration when pumping at 1064nm with power $P_0 = 500\text{W}$. (a) Effective area of the sensor (b) Maximum gain of the sensor; (c) anti-Stokes (blue) and Stokes (red) wavelengths for sensor (solid) and activated sensor (dashed); (d) Shift of the anti-Stokes (blue) and Stokes (red) wavelengths.

6. Verification of operation through direct numerical modelling

We now verify the predicted sensitivity through direct numerical modelling. Since we deal with long picosecond (ps) pulses and want fiber lengths just long enough to generate a detectable Stokes and anti-Stokes line, but short enough to avoid any other nonlinear effects, such as supercontinuum generation [37], we can neglect the Raman effect, self-steepening, and linear loss. This simplifies the model to the standard Nonlinear Schrödinger (NLS) equation with full dispersion [9]

$$i\frac{\partial A}{\partial z} + \sum_{m=2}^{\infty} \frac{i^m \beta_m}{m!} \frac{\partial^m A}{\partial T^m} + \gamma |A|^2 A = 0. \quad (3)$$

Here $A = A(z, t)$ is the envelope of the optical field and β_m are the dispersion parameters already defined. The nonlinear coefficient is $\gamma = n_2 \omega_0 / (c A_{\text{eff}})$ where $n_2 = 2.6 \times 10^{-20} \text{m}^2/\text{W}$ for silica and the pump wavelength is $\lambda_0 = 1064 \text{nm}$. The effective area will be given at each simulation. Time t is as usual measured in a frame of reference moving with the group-velocity of the carrier wave [9]. We pump with a Gaussian shaped pulse with an intensity full width at half maximum (FWHM) of 7ps. The initial condition is therefore

$$A(0, t) = \sqrt{P_0} \exp\left(-\frac{t^2}{2T_0^2}\right) \quad (4)$$

where $P_0 = 500 \text{W}$ is the peak power and $T_0 = 7 \text{ps} / \sqrt{\ln(16)}$. We use a split-step fourier method programmed in Matlab with $N_t = 2^{18}$ discretization points and a time window of 80 pulse widths. The temporal resolution is thus $dt = 80T_0/N_t = 1.3 \text{fs}$. We use a constant steplength short enough to conserve the energy to within 10^{-10} of the initial value for all runs. Finally we use a noise seed of one-photon per mode [38, 39].

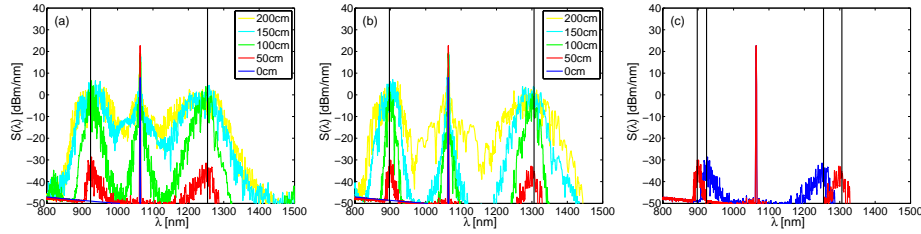


Fig. 11. Evolution of the power spectral density, $S(z, \lambda)$, in a MOF with hole size $d=1.75 \mu\text{m}$ and $\Lambda=2.56 \mu\text{m}$ (optimum in water configuration), pumped at 1064nm with 7ps intensity FWHM pulses with 500W peak power at a repetition rate of 80MHz. $S(z, \lambda)$ at different propagation lengths for the sensor (a) and the activated sensor (b). (c) $S(z, \lambda)$ after $z=50 \text{cm}$ for the sensor (blue) and the activated sensor (red). Vertical lines are MI predictions.

In our optimization we found that the best sensor performance is obtained in the water configuration with a MOF with hole size $d = 1.75 \mu\text{m}$ and pitch $\Lambda = 2.56 \mu\text{m}$. For this fiber the effective area is $A_{\text{eff}} = 8.16 \mu\text{m}^2$ for the sensor and $A_{\text{eff}} = 8.22 \mu\text{m}^2$ for the activated sensor. We keep the moderate peak power $P_0=500 \text{W}$, knowing that the gain can always be increased by increasing the power. The results are shown in Fig. 11, where we plot the power spectral density $S(z, \lambda)$, defined as

$$\int_{\lambda_{\min}}^{\lambda_{\max}} S(z, \lambda) d\lambda = P_{\text{av}} \Rightarrow S(z, \lambda) = \frac{c f_{\text{rep}}}{\lambda^2} |\tilde{A}(z, \nu)|^2, \quad (5)$$

where $\nu = c/\lambda$ is the frequency and f_{rep} is the repetition rate of the pump laser. Thus the integral over the available wavelength regime of the power spectral density is the average power of the

pump laser. Here we assume a repetition rate of $f_{\text{rep}}=80\text{MHz}$. The tilted noise floor is due to the one-photon-per-mode seed. In the plotting the spectra have been averaged. The numerical results show that in the sensor the anti-Stokes and Stokes waves are generated around 923.7nm and 1254.5nm, respectively. In the activated sensor we observe that the anti-Stokes and Stokes waves are generated around 897.5nm and 1306.3nm, respectively. This give a Stokes shift of 52nm, which confirms the predictions of our MI calculations from Fig. 10.

7. Conclusion

In conclusion we have demonstrated that truly label-free and selective fiber-optical biosensing is possible using the nonlinear process of modulational instability (MI) in a microstructured optical fiber (MOF). The detection process is carried out inside the holes of the MOF and the nonlinearity is inherent to the fiber. This means that the sensor is highly robust and that no post-processing of the fiber is necessary. The sensor operates by detecting the center wavelength of the Stokes (or anti-Stokes) band generated by MI and how it shifts when the sensor captures a layer of biomolecules. We show that optimum sensor operation with a maximum shift requires pumping close to the zero-dispersion wavelength of the MOF.

Considering as an example a standard triangular MOF and pumping at 1064nm we have devised appropriate design guidelines for optimizing the sensor for maximum shift and maximum MI gain. In the air configuration, where the holes are pumped through with air after sampling, we found the optimum hole structure to have a hole diameter of $d = 1.00\mu\text{m}$ and a pitch of $\Lambda = 2.80\mu\text{m}$, leading to a shift of 60nm with a gain of 24dB/m. In the water configuration, where the holes are flushed through with water after sampling, we found the optimum diameter and pitch to be $1.75\mu\text{m}$ and $2.56\mu\text{m}$, respectively, leading to a shift of 52nm with a gain of 40dB/m. These shifts were obtained with a peak pump power of 500W, but we have shown that choice of pump power is not critical and that the pump power may be increased to increase the gain, without significant penalty in the shift. We note, however, that at high powers the heating of the sensor due to the pumping, could become an issue that would need to be taken into consideration.

Opting for larger holes to ease bio-chemical reaction procedures and reduce preparation time and for maximum gain to get a good detectable signal in as short a length as possible, we have finally used direct numerical modelling to verify the operation of the sensor in the predicted optimum water configuration with $d = 1.75\mu\text{m}$ and $\Lambda = 2.56\mu\text{m}$. Our results verified that indeed a Stokes shift of 52nm due to the capture of a 5nm thick layer of biomolecules could be achieved and detected in a 50cm MOF. This corresponds to a sensitivity of 10.4nm/nm, which is 7.5 times better than the hitherto only reported label-free fiber-optical biosensor [28]. With the standard 5 rings of holes this optimum 50cm MOF would require 100 nanoliter of sample.

Using the resonant generation of Stokes and anti-Stokes waves through MI is not limited to biosensing, but can of course equally well be applied to refractive index sensing, just as for example MOF sensors based on Bragg or long-period grating [27].

Acknowledgments

We would like to thank Lars H. Pedersen from Bioneer A/S for discussions about the appropriate thickness of the bilayers and Michael Frosz for discussions about the simulations.